

pubs.acs.org/Macromolecules Article

Molecular Simulations Revealing Effects of Non-concatenated Ring Topology on Phase Behavior of Symmetric Diblock Copolymers

Andrew Wijesekera, Daniel L. Vigil, and Ting Ge*



ACCESS I

Cite This: https://doi.org/10.1021/acs.macromol.3c02473

Metrics & More



Article Recommendations

Non-Concatenated Di-block Ring Polymers in Lamellar Phase
Original Conformations

Post-PPA Conformations

ABSTRACT: The distinctiveness of nonconcatenated ring polymers, as manifested in their fractal globular conformations and selfsimilar dynamics with no long-lived entanglement network, propels the idea of using ring topology to transform the phase behavior of block copolymers. With limited experimental studies of high-molecular-weight diblock ring polymers, large-scale molecular simulations of symmetric diblock copolymers are used to investigate the effects of nonconcatenated ring topology on their phase behavior. The absence of an entanglement network facilitates the phase-separation kinetics, suggesting relative ease in processing diblock ring polymers. The more compact globular conformations of ring polymers with respect to the Gaussian random-walk conformations require a higher enthalpic repulsion to drive the lamellar phase separation. Compared with the mean-field theory for the order-disorder transition in Gaussian diblock ring polymers, the simulations demonstrate the necessity for a new theory incorporating both the effects of fluctuations and the topological invariance of nonconcatenation. In the strong segregation regime, diblock ring polymers are stretched near the lamellar interface but with the globular conformational statistics preserved at larger length scales. The lamellar spacing d increases with enthalpic repulsion between the two blocks as well as the molecular weight of the diblock ring. The scaling argument for d of diblock linear polymers is modified by accounting for the globular conformations and predicts well the dependencies of d on the enthalpic repulsion and molecular weight. The lamellar interface becomes sharper as the enthalpic repulsion increases. While the theory predicts that the intrinsic interfacial width does not depend on the polymer molecular weight or topology, the apparent interfacial width w, which is broadened by the capillary wave, exhibits slight variation with the molecular weight and topology.

1. INTRODUCTION

The phase behavior of block copolymers underlies many technological applications that rely on the morphology of block copolymers, such as lithography, water purification, gas permeation, and ion transport in batteries. ^{1–6} Predicting the phase behavior of block copolymers has been celebrated as a triumph of polymer field theory. ^{7–22} Much of the parameter space, including the molecular weight, block composition, enthalpic interaction strength, and polymer architecture, has been extensively explored. One promising direction to expand the parameter space is to replace the conventional linear chains with nonconcatenated rings. ^{23–27} Such an expansion is intriguing due to the distinctive conformations, ^{28–35} dynamics, ^{33,36–42} and material properties ^{43–47} revealed for homopolymer rings in the past two decades and also timely because of

the advances in synthesizing and characterizing high-molecular-weight ring polymers. $^{48,49}\,$

Supporting Information

Molecular simulations with precise control of ring polymer topology and unique access to microscopic details are well positioned to guide the expansion of the block copolymer design space using nonconcatenated ring topology. Existing simulations on the phase behavior of diblock ring polymers^{50,51}

Received: November 29, 2023 Revised: February 22, 2024 Accepted: March 5, 2024



have been limited to the chain length N smaller or moderately larger than the entanglement length $N_{\rm e}$ of a linear polymer melt. Nevertheless, as demonstrated in the comparisons of linear and ring homopolymers, ring polymers differ more distinctively from linear polymers as N becomes much larger than $N_{\rm e}.^{28,33,35-37,42}$ Specifically, the topological constraints of nonconcatenation make the ring polymers with $N/N_{\rm e}\gg 1$ more compact compared to the linear polymers of the same N, and the resulting average ring polymer size scales as $N^{1/3}$ rather than $N^{1/2}$ for the linear polymers. The limited overlap of the compact ring polymers prevents the formation of a long-lived entanglement network, and thus the ring polymer dynamics is faster than the dynamics of entangled linear polymers, exhibiting no rubbery plateau in the stress relaxation function. $^{33,36-42}$

In this paper, large-scale molecular simulations are performed to investigate the phase behavior of symmetric diblock ring polymers with $N/N_{\rm e}$ up to O(10). The simulations reveal the effects of nonconcatenated ring topology on the order—disorder transition and the static properties of the ordered lamellar phase. The topology effects observed for diblock rings are consistent with how the nonconcatenation topological invariants transform the conformations and dynamics of homopolymer rings. Section 2 describes the simulation model and methods for the simulations of diblock copolymer phase behavior. Section 3 reports the results of the molecular simulations and the accompanying theoretical analysis. The paper concludes with Section 4, where a summary of key findings is presented with remarks.

2. MODEL AND METHODS

The coarse-grained bead—spring model of polymer 52 is used in the simulations. All beads of size σ and mass m interact via the truncated, shifted, and purely repulsive Lennard-Jones (LJ) potential with the interaction strength ϵ . $U_{\rm LJ}(r)=4\epsilon[(\sigma/r)^{12}-(\sigma/r)^6]+\epsilon$, for r smaller than the cutoff distance $r_{\rm c}=2^{1/6}\sigma\approx 1.12\sigma$, and corresponds to purely repulsive interaction. Neighboring beads along the polymer chain are connected by a finite extensible nonlinear elastic (FENE) potential. $U_{\rm FENE}(r)=-(kR^2/2)\ln[1-(r/R)^2]+4\epsilon[(\sigma/r)^{12}-(\sigma/r)^6]+\epsilon$ with $k=30\epsilon/\sigma^2$ for $r< R=1.5\sigma$. For two neighboring bonds along the polymer chain, there is a bond-bending potential $U_{\rm bend}(\theta)=k_{\theta}(1+\cos\theta)$, where θ is the angle between the two bonds and the bending stiffness $k_{\theta}=1.5\epsilon$, which gives $N_{\rm e}=28.^{53,54}$

M polymers, each of which consisted of N beads, were placed in a cubic simulation box with periodic boundary conditions. Five systems of nonconcatenated ring polymers R50, R100, R200, R400, and R800 of $N=50(1.8N_{\rm e}),\ 100(3.6N_{\rm e}),\ 200(7.2N_{\rm e}),\ 400(14N_{\rm e}),\$ and $800(29N_{\rm e}),\$ respectively, were simulated. As a comparison, two linear polymer systems L50 and L400 of $N=50(1.8N_{\rm e})$ and $400(14N_{\rm e})$, respectively, were simulated. The values of N and M, the polymer radius of gyration R_g , and the size of the simulation box L are listed in Table 1. The total number of beads ranged from $M\times N=8\times 10^4$ to 6.4×10^5 , which was chosen to enable large-scale simulations of

Table 1. Parameters for Simulation Samples

	chain length N	number of chains M	radius of gyration $R_{ m g}(\sigma)$	simulation box size $L(\sigma)$
R50	50	4000	3.0	61.7
R100	100	800	4.1	45.4
R200	200	200	5.6	36.1
R400	400	200	7.3	45.4
R800	800	400	9.4	72.1
L50	50	2000	4.6	48.9
L400	400	1600	13.4	90.9

sample equilibration and phase behavior under various conditions with the computing resources available. The number density of monomers is $\rho=0.85\sigma^{-3}$ in all systems. The simulation box size L is greater than $6R_{\rm g}$. Following the standard protocols, ^{28,37} each system was equilibrated at temperature $T=1.0\epsilon/k_{\rm B}T$ using a Nosé–Hoover thermostat with a characteristic damping time $1\tau=1\sigma\sqrt{m/\epsilon}$. The time step for integrating the equations of motion was 0.01τ .

To simulate symmetric diblock copolymers, monomers in two halves of a polymer are assigned two different types, A and B. The strength of the LJ interaction between two monomers of the same type is identical, and $\epsilon_{\rm AA}=\epsilon_{\rm BB}=\epsilon$. The strength of the repulsive LJ interaction $\epsilon_{\rm AB}$ between two monomers of different types is increased above ϵ to introduce incompatibility, as in previous simulations of heterogeneous polymer systems. The effect of $\epsilon_{\rm AB}=(\epsilon_{\rm AB}-(\epsilon_{\rm AA}+\epsilon_{\rm BB})/2]/\epsilon$ quantifies the strength of the enthalpic repulsion and may be mapped to the χ parameter in the classical Flory–Huggins theory. The model-independent universality in the phase behavior of symmetric block copolymer melts has been demonstrated by Glaser et al. 60

At each $\tilde{\epsilon}$, a diblock copolymer melt was equilibrated through a two-step process. In the first step, the temperature $T = 1.0\epsilon/k_{\rm B}$ was maintained via a Nosé-Hoover thermostat with a characteristic damping time of 1τ , and the volume of the simulation box was constant. The ordered lamellar phase emerged at sufficiently large $\tilde{\epsilon}$. The phase separation in the simulations did not always result in lamellar domains, with the interface lying in the xy-plane. In some cases, the x, y, and z coordinates were permutated to allow the phase separation to be in the z-direction. For diblock linear polymers, to accelerate the phase separation with respect to pure molecular dynamics, pairs of bonds may be swapped via the Monte Carlo (MC) rules with the Boltzmann acceptance criterion. 61 The bond-swapping process permits the crossing of linear polymer chains and thereby accelerates the polymer dynamics with respect to the slow entangled dynamics, where the chains cannot cross each other. This acceleration algorithm is known as "double bridging" and is realized by the "fix bond/swap" command in the LAMMPS package. 62 In the second step of the equilibration process, the dimensions of the melt sample after the first step were adjusted by applying a constant pressure along the *z*-direction and an independent constant pressure within the *xy*-plane. The box size L_z varied at $P_z = 5.1\epsilon/\sigma^3$, while the box sizes L_x and L_y were coupled to vary simultaneously at $P_x = P_y = 5.1\epsilon/\sigma^3$. The strength of the pressure was chosen to maintain the monomer density at $0.85\sigma^{-3}$. The pressure control was performed using a Nosé-Hoover barostat with a characteristic damping time of 10τ . Meanwhile, the temperature was kept at $T = 1.0\epsilon/k_B$ using the same thermostat. In the second step of equilibration, the pressure component normal to the lamellar interface is controlled independently from the other two components within the interface. Without the first step, where the symmetry of the three axes is broken, one would not know which direction lies normal to the lamellar interface and thus could not apply the pressure control to adjust the box dimensions appropriately. After the two-step equilibration, the lamellar spacing d for strongly segregated diblock copolymers was calculated as $\langle L_z \rangle/2n$, where $\langle L_z \rangle$ is the average box size along a dynamics trajectory of $10^4\tau$ at constant pressure and n is the number of periods. All simulations were performed using the LAMMPS

Primitive path analysis (PPA)⁵³ was used to analyze the topology of simulated polymers. In the original PPA of homopolymer linear chains, the two ends of a chain are fixed, while bond tension is introduced to reduce the chain contour length as much as possible without crossing nearby chains. This protocol leads to the emergence of the chain's primitive path, as defined in the tube model of entangled polymer dynamics. For diblock copolymers in this work, PPA was performed by fixing the two ends of each block in space, corresponding to four fixed beads per copolymer.

3. RESULTS

3.1. Phase-Separation Kinetics. The phase separation from a disorder melt of symmetric diblock copolymers to a

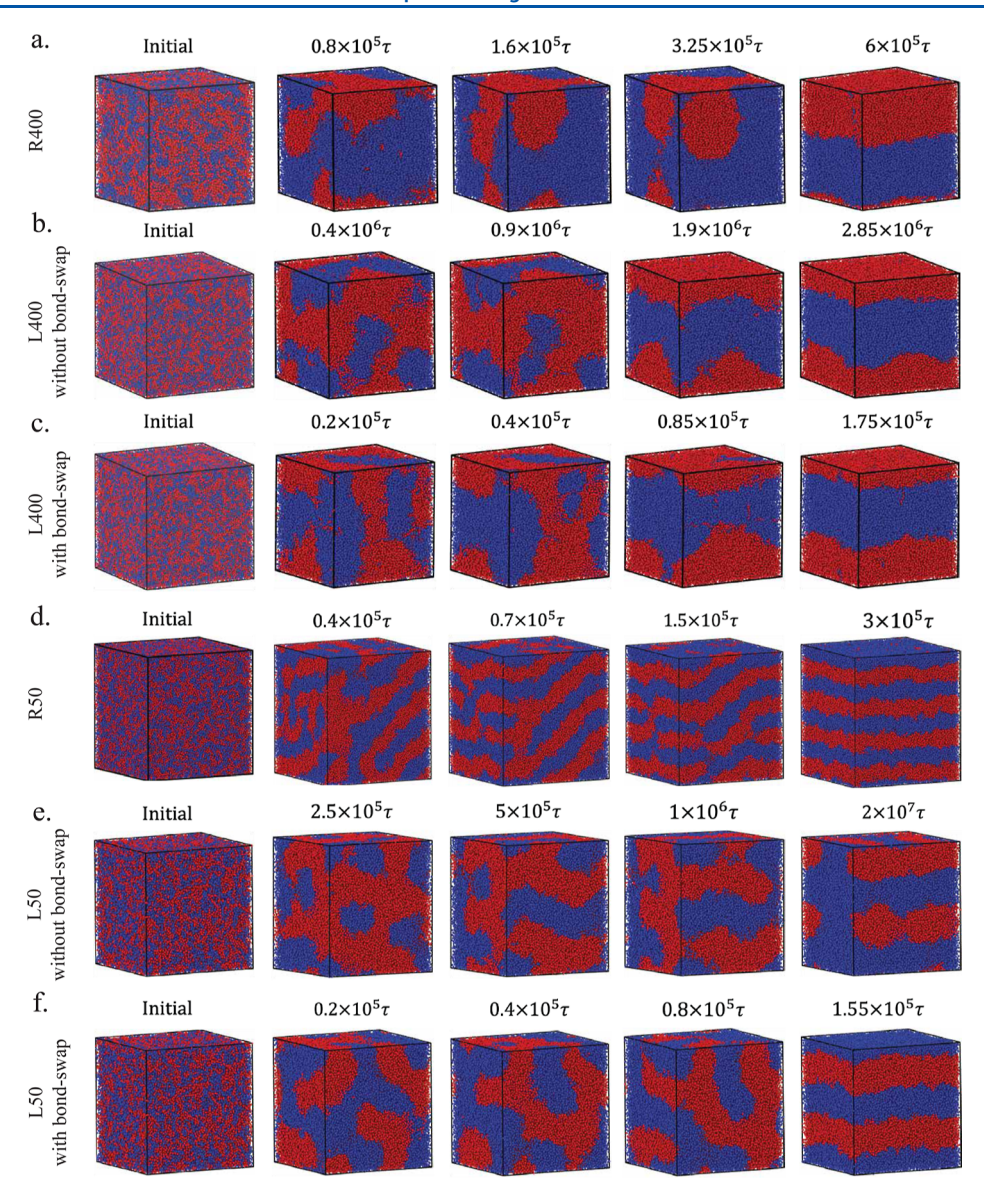


Figure 1. Morphologies of (a) R400, (b) L400 without bond-swap, (c) L400 with bond-swap, (d) R50, (e) L50 without bond-swap, and (f) L50 with bond-swap at different stages of the phase-separation simulations. $\tilde{\epsilon}=3.0$ for N=400, while $\tilde{\epsilon}=5.0$ for N=50. Red and blue indicate the monomers of types A and B, respectively.

periodic lamellar structure is observed during the first step of the two-step equilibration when $\tilde{\epsilon}$ is sufficiently large. Figure 1a illustrates the evolution of the melt morphology for R400 at $\tilde{\epsilon}$ = 3.0. There is a transition from the disordered state with wellmixed A (red) and B (blue) monomers to the lamellar phase with separated red and blue domains. To characterize the morphology, the order parameter $\psi(\tilde{z}) = [\phi_{A}(\tilde{z}) - \phi_{B}(\tilde{z})]/[\phi_{A}(\tilde{z}) + \phi_{B}(\tilde{z})]$, where $\phi_{A}(\tilde{z})$ and $\phi_{\rm R}(\tilde{z})$ are the volume fractions of A and B monomers, respectively, is calculated as a function of $ilde{z} = (z-z_{
m min})/(z_{
m max}-z_{
m min})$, where $z_{
m max}$ and $z_{
m min}$ are the upper and lower bounds of the z-coordinates, respectively. Figure 2a shows the time evolution of $\psi(\tilde{z})$ for R400 at $\tilde{\epsilon} = 3.0$, which parallels the snapshots in Figure 1a. The snapshots for morphology evolution and the corresponding order parameter plots for L400 at $\tilde{\epsilon}$ = 3.0 are shown in Figures 1b and 2b, respectively. Comparing the phase separations in R400 and L400, one sees that the separation kinetics are faster in the

diblock rings. The lamellar phase is well developed after $6 \times 10^5 \tau$ and $2.85 \times 10^6 \tau$ for R400 and L400 at $\tilde{\epsilon} = 3.0$, respectively. Note that the snapshots at intermediate stages correspond roughly to 1/8, 1/4, and 1/2 of the entire trajectory of phase separation.

The faster phase separation in diblock rings agrees with the faster dynamics of homopolymer rings, 33,36,37,42 both arising from the absence of a long-lived entanglement network. The time scale for the lamellar phase separation in the simulations is comparable to the diffusion time $\tau_{\rm D}$ of the corresponding homopolymers, which is $2.38 \times 10^5 \tau$ and $5.97 \times 10^6 \tau$ for the rings and linear chains of N=400, respectively. The diditional use of the bond-swap MC algorithm accelerates the phase separation in diblock linear polymers. As shown in Figures 1c and 2c, with a bond-swap, the lamellar phase is well developed after a much shorter time of $1.75 \times 10^5 \tau$ for L400 at $\tilde{\epsilon}=3.0$, which is even faster than the phase separation in R400.

The contrasting topology of diblock polymers in L400 and R400 is demonstrated by PPA. Consider PPA of the disorder

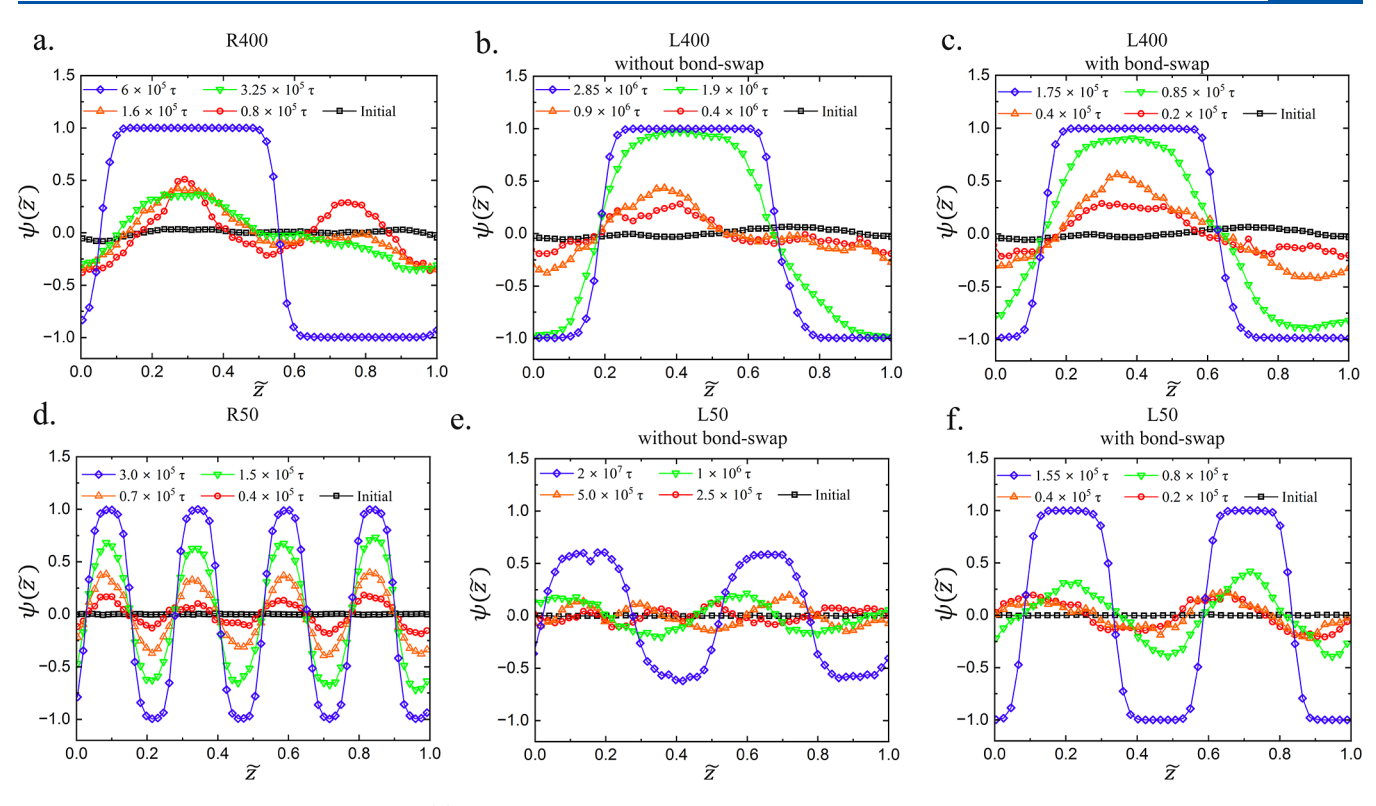


Figure 2. Profiles of the order parameter $\psi(\tilde{z})$ for the same systems as in Figure 1.

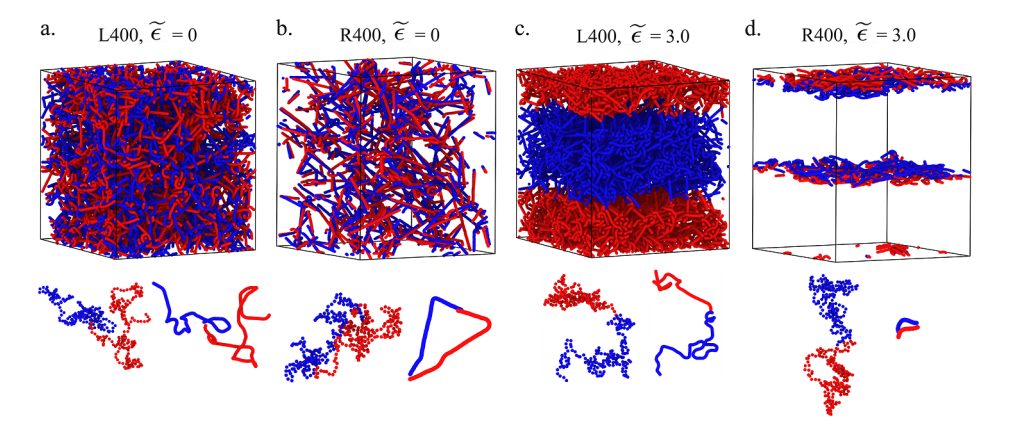


Figure 3. Post-PPA snapshots of L400 and R400 in the disorder state with $\tilde{\epsilon}=0$ and the strongly segregated state with $\tilde{\epsilon}=3.0$. Red and blue indicate the two types of monomers. In each case, the original and post-PPA conformations of one diblock polymer are highlighted.

state at $\tilde{\epsilon} = 0$ first. For a diblock linear chain, with two ends of each block fixed, the reduction to straight segments connecting the four fixed beads is hindered by nearby linear chains due to the strong mutual overlap in a well-entangled system. By contrast, the reduction to straight segments connecting the four fixed beads, which essentially are the two fixed junctions between A and B blocks, is less hindered by nearby rings, as their mutual overlap is limited due to the nonconcatenation constraints. As a result, more contour lengths are removed after the PPA of diblock rings, leading to more unfilled space in the post-PPA simulation box. See the comparison shown in Figure 3a,b. The post-PPA snapshots of L400 and R400 at $\tilde{\epsilon}$ = 3 show an even higher contrast. For a diblock linear chain in the lamellar phase, two of the four fixed beads are located at an interface between lamellar domains, while the other two are away from the interface. The post-PPA snapshot in Figure 3c shows that the primitive paths are well entangled as in Figure

3a, but the blue and red primitive paths are segregated. For a diblock ring in the lamellar phase, all four fixed beads are located at an interface. As a result, the primitive paths are confined to the two interfaces, as illustrated in Figure 3d. The contour length reduction in this case resembles pulling taut shoelaces over the array of holes on a sneaker, visualizing the consequence of nonconcatenation.

While there is only one lamellar period in the simulation box for N=400, multiple lamellar periods develop for $N\leq 100$ with the selected simulation box dimensions. Figures 1d and 2d show the phase separation in R50 at $\tilde{\epsilon}=5.0$. The lamellar phase with four periods is well developed after $3\times 10^5\tau$. Previous simulations³⁷ have determined the diffusion time to be $\tau_{\rm d}=7\times 10^3\tau$ for the homopolymer rings of N=100 in the melt state. $\tau_{\rm d}$ for the homopolymer rings of N=50 is expected to be smaller than $7\times 10^3\tau$. As a result, the time it takes to complete the phase separation in R50 at $\tilde{\epsilon}=5.0$ is much longer

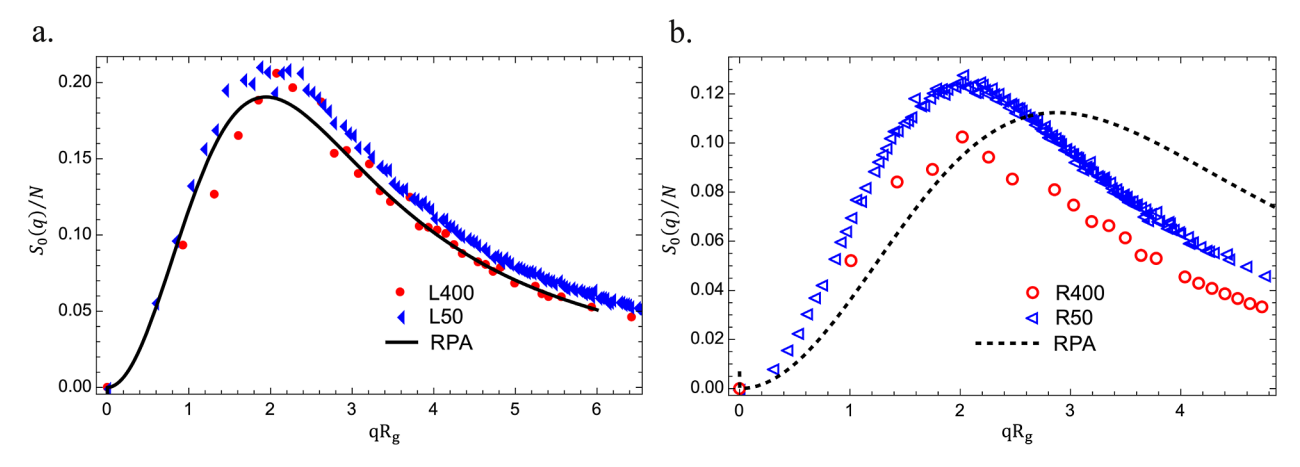


Figure 4. $S_0(q)/N$ as a function of qR_g for (a) L50 and L400 and (b) R50 and R400. The solid and dashed lines are the predictions of Leibler's and Marko's RPA theories for diblock linear and ring polymers, respectively.

than τ_{D} of the corresponding homopolymer rings. This is in contrast to the result that the two time scales are comparable for the phase separation in R400 at $\tilde{\epsilon} = 3.0$. The difference arises from the need to accommodate multiple lamellar periods in the simulations of shorter diblock polymers. The phase separation in L50 is also affected by the accommodation of multiple lamellar periods. Figures 1e and 2e show that the phase separation in L50 at $\tilde{\epsilon} = 5.0$ involves two lamellar periods and is not completed by $2 \times 10^7 \tau$. The longest time in the simulation is much longer than the diffusion time $\tau_{\rm d}$ of the homopolymer linear chains of N = 50 in the melt state, which is expected to be smaller than $\tau_d = 4.8 \times 10^4 \tau$ for $N = 100.3^{\circ}$ This long simulation time is demanding from the perspective of computing resources. Therefore, the use of the bond-swap MC algorithm is necessary to complete phase separation. As shown by Figures 1f and 2f, with the acceleration algorithm, the lamellar phase in L50 at $\tilde{\epsilon} = 5.0$ is well developed after 1.55 \times 10⁵ τ , saving much computing time.

The results in Figures 1 and 2 for phase-separation kinetics are limited to only four samples, but they reflect the faster kinetics of nonconcatenated diblock rings with respect to diblock linear chains, as well as the effects of multiple lamellar periods on the kinetics. A systematic study of the phase-separation kinetics, particularly with multiple lamellar periods, is out of the scope of this study using molecular simulations. Computational methods beyond molecular simulation would be needed to tackle the larger length scales and longer time scales of the phase separation with multiple lamellar periods. The simulation data reported in the following subsections are for the samples after the two-step equilibration process. Specifically, pure molecular dynamics were performed for the diblock ring polymers, while molecular dynamics coupled with the bond-swap MC algorithm were performed for the diblock linear chains in the first step of the equilibration.

3.2. Order–Disorder Transition Point. To determine the order–disorder transition (ODT) point, $\tilde{\epsilon}$ is systematically varied in the simulations. The systems R50, L50, R400, and L400 are studied in detail below. Following scattering experiments and field theories of ODT, the structure factor S(q) in the simulations is examined. The structure factor is computed as

$$S(q) = \sum_{i,j=1}^{M \times N} b_i b_j \langle \exp[i\vec{q} \cdot (\vec{r}_i - \vec{r}_j)] \rangle / \sum_{i=1}^{M \times N} b_i^2$$
(1)

where b_i and $\vec{r_i}$ are the scattering length and the position of monomer i, respectively. The wavevector $\vec{q}=(2\pi/L)(n_x,n_y,n_z)$, where n_x , n_y , and n_z are integers. $b_i=1$ for all monomers of type A, while $b_i=-1$ for type B. For one simulation sample at a given $\tilde{\epsilon}$, S(q) is averaged over $O(10^3)$ frames along a trajectory at constant temperature and constant volume, and the time interval between two frames is 1000τ .

 $S_0(q)$ is the structure factor in the disorder phase with $\tilde{\epsilon}=0$. $S_0(q)$ for the simulation samples R50, L50, R400, and L400 are shown in Figure 4 and compared with the predictions of the mean-field theory based on the random phase approximation (RPA). For diblock linear polymers, Leibler's RPA theory predicted

$$S_{\rm L}(q)/N = 1/[F_{\rm L}(qR_{\rm g}) - 2\chi N]$$
 (2)

where

$$F_{L}(x) = (x^{4}/8)$$
$$[x^{2}/4 + \exp(-x^{2}/2) - \exp(-x^{2})/4 - 3/4]^{-1}$$

The RPA prediction for $NS_0^{-1}(q)$ at $\chi=0$ is shown by the solid line in Figure 4a. The peak value of $S_0(q)/N$ is $S_0(q^*)/N=0.19$ at $q^*R_{\rm g}=1.95$. Compared with the RPA prediction, the peak position of $S_0(q)/N$ is also around $q^*R_{\rm g}=1.95$ for both L50 and L400. However, the numerical result of $S_0(q)/N$ deviates from the RPA prediction. The deviation may be accounted for by the non-mean-field renormalization-one-loop (ROL) theory, ¹⁸ but a detailed evaluation of the ROL theory is outside the scope of this work.

For diblock ring polymers, Marko's RPA theory¹³ predicted

$$S_{\rm R}(q)/N = 1/[F_{\rm R}(qR_{\rm g}) - 2\chi N]$$
 (4)

where

$$F_{R}(x) = \{4[1 - \exp(-x^{2}/4)]/x^{2} - \sqrt{\pi/x^{2}} \exp(-x^{2}/4)\operatorname{erfi}(x/2)\}^{-1}$$
(5)

As shown by the dashed line in Figure 4b, the RPA theory predicts that the peak value of $S_0(q)/N$ is $S_0(q^*)/N = 0.11$ at $q^*R_{\rm g} = 2.88$. By contrast, $S_0(q)/N$ in the simulations peaked at $q^*R_{\rm g} \approx 2 < 2.88$. Moreover, the exact shape of $S_0(q)/N$ deviates from the RPA prediction. The topological constraints of nonconcatenation are absent in Marko's RPA theory, which

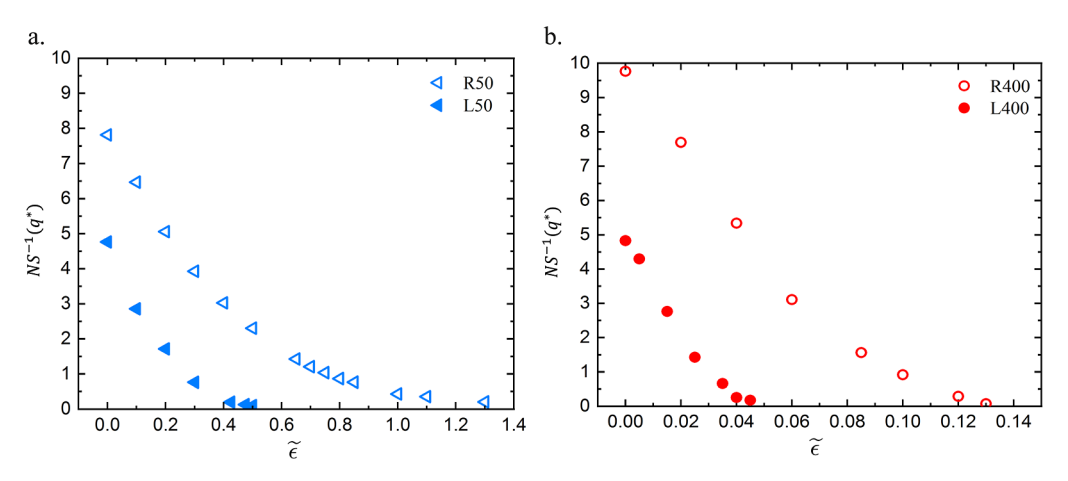


Figure 5. $NS^{-1}(q^*)$ as a function of $\tilde{\epsilon}$ for (a) R50 and L50 and (b) R400 and L400.

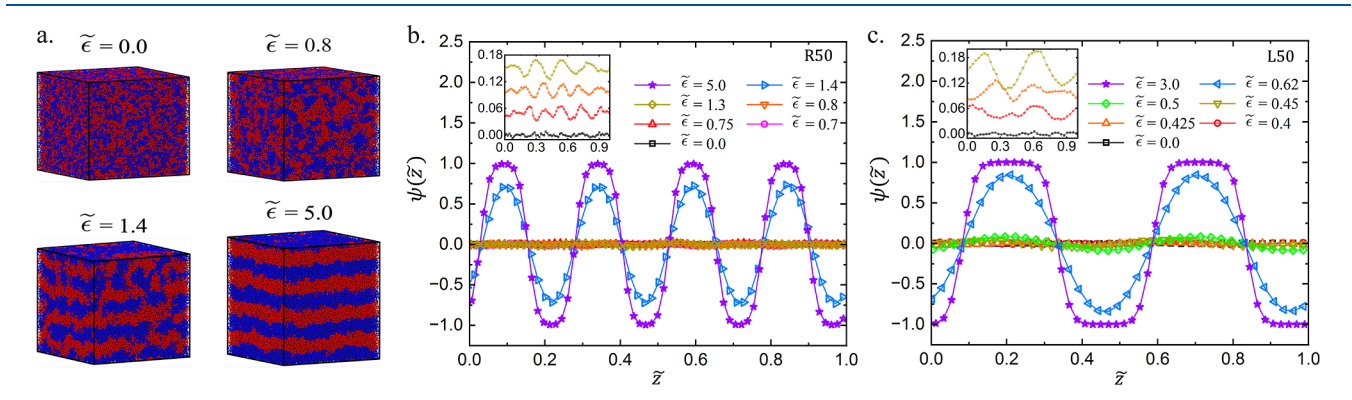


Figure 6. (a) Snapshots of diblock ring polymers of N=50 at different $\tilde{\epsilon}$ with red and blue indicating two types of monomers. The profiles of the order parameter $\psi(\tilde{z})$ at indicated interaction strength $\tilde{\epsilon}$ for (b) diblock ring polymers and (c) diblock linear polymers of N=50. The insets are enlarged views of the profiles at $\tilde{\epsilon}=0$ and near the ODT. For clarity, there is a consecutive vertical shift by 0.05 in the insets.

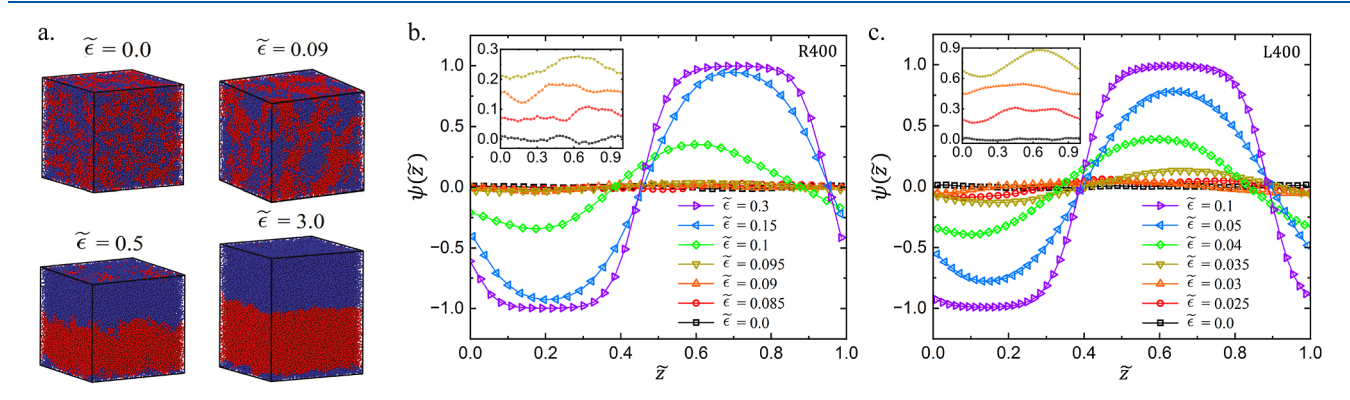


Figure 7. (a) Snapshots of diblock ring polymers of N=400 at different \tilde{e} with red and blue indicating two types of monomers. The profiles of the order parameter $\psi(\tilde{z})$ for the diblock (b) ring and (c) linear polymers of N=400 at indicated interaction strength \tilde{e} . The insets are enlarged views of the profiles in the disordered phase and near the ODT. For clarity, there is a consecutive vertical shift by 0.08 and 0.24 in the insets of (b,c), respectively.

models ring polymers simply as "phantom" Gaussian random-walk rings that can cross one another. The nonconcatenation topological constraints force the rings to adopt globular conformations, which are more compact than the Gaussian random-walk rings. Such a globular conformation has been theoretically described as a self-similar fractal loopy globule 33 and confirmed by recent scattering experiments. 35,42 New analytical theories need to be developed to capture the $S_0(q)/N$ of nonconcatenated diblock rings.

The peak value of S(q)/N at q^* rises with increasing $\tilde{\epsilon}$ and diverges at $\tilde{\epsilon}_{\text{ODT}}$. The decrease of $NS^{-1}(q^*)$ toward 0 is used to estimate $\tilde{\epsilon}$. As shown in Figure 5, $NS^{-1}(q^*)$ first decreases linearly with increasing $\tilde{\epsilon}$, and then the decrease slows as the ODT is approached. For diblock linear polymers, the linear decrease of $NS^{-1}(q^*)$ is predicted by the RPA theory. The slowdown in the decrease toward ODT may be described by including the effects of non-mean-field fluctuations, as in the Fredrickson–Helfand theory and the ROL theory. For diblock ring polymers, there is also a linear decrease followed

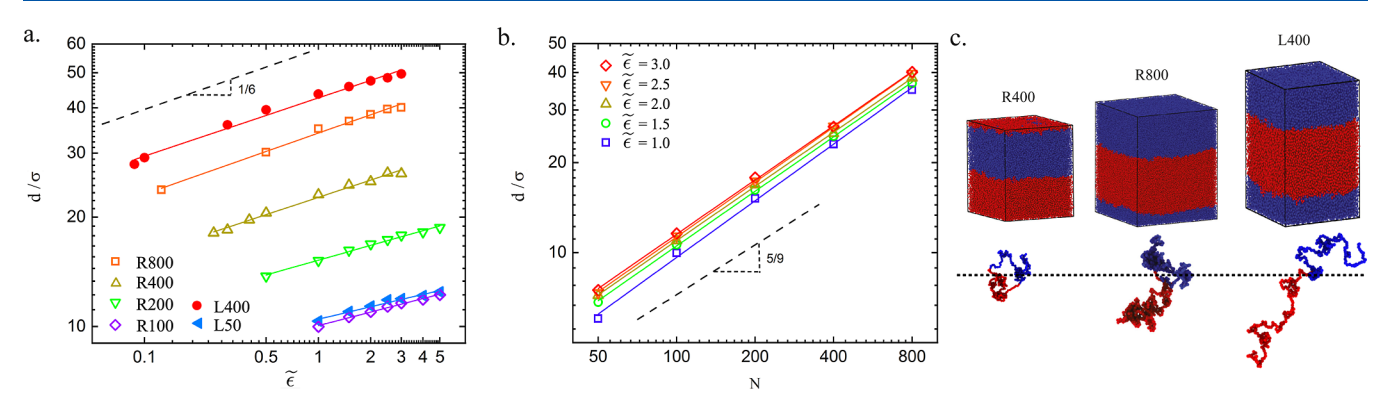


Figure 8. Lamellar spacing d as functions of (a) $\tilde{\epsilon}$ and (b) N for the diblock polymer samples in the strong segregation regime. Solid lines in (a,b) indicate the best fit to the power-law functions $d \sim \tilde{\epsilon}^a$ and $d \sim \tilde{\epsilon}^\nu$, respectively. Dashed lines indicate the corresponding predictions of scaling theory. (c) Snapshots of R400, R800, and L400 at $\tilde{\epsilon} = 3.0$, where an enlarged view of one selected diblock copolymer is shown in each case. The dashed line indicates the midplane of the lamellar interface.

by a slowdown in the decrease as ODT is approached. New theories need to be developed to describe the decrease of $NS^{-1}(q^*)$ with increasing $\tilde{\epsilon}$ in diblock ring polymers. From the vanishing of $NS^{-1}(q^*)$ in Figure 5, $\tilde{\epsilon}_{\rm ODT}$ is estimated to be 1.3, 0.475, 0.13, and 0.045 for R50, L50, R400, and L400, respectively. As the onset of the ODT is approached by increasing $\tilde{\epsilon}$ from 0 in the simulations, there is a metastability of the disorder phase that retards the emergence of the lamellar order. Therefore, the estimate of $\tilde{\epsilon}_{\rm ODT}$ above is the upper bound of the actual $\tilde{\epsilon}_{\rm ODT}$.

The lower bound of $\tilde{\epsilon}_{ODT}$ in the simulations is obtained by reducing $\tilde{\epsilon}$ from a sufficiently large value, where a wellseparated lamellar phase exists, and then monitoring the decay of the order parameter profile $\psi(\tilde{z})$. This approach gives the lower bound because the metastability of the lamellar phase slows down the decay of $\psi(\tilde{z})$ as ODT is approached. Snapshots of R50 and R400 at selected $\tilde{\epsilon}$ are shown in Figures 6a and 7a. As $\tilde{\epsilon}$ decreases, there is a transition from the lamellar phase to the disorder phase. Figure 6b,c shows $\psi(\tilde{z})$ for R50 and L50. Each line of $\psi(\tilde{z})$ is the average of 100 instantaneous frames separated with an interval of 1000τ in the equilibrated state. $\psi(\tilde{z})$ exhibits a periodic structure that indicates the lamellar order at sufficiently large $\tilde{\epsilon}$. $\psi(\tilde{z})$ is almost flat at $\tilde{\epsilon} = 0$, indicating no order. $\psi(\tilde{z})$ near ODT is shown in the insets of Figure 6b,c. The breakdown of the periodic features of $\psi(\tilde{z})$ is observed by $\tilde{\epsilon}_{ODT} = 0.8$ and 0.425 for R50 and L50, respectively. Similarly, Figure 7b,c shows $\psi(\tilde{z})$ for R400 and L400 with enlarged views of $\psi(\tilde{z})$ near ODT in the insets. The lower bound of $\tilde{\varepsilon}_{ODT}$ is estimated as 0.09 and 0.03 for R400 and L400, respectively.

Combining the estimated upper and lower bounds, $\tilde{\epsilon}_{\text{ODT}}$ is located in (0.8, 1.3), (0.425, 0.475), (0.09, 0.13), and (0.03, 0.045) for R50, L50, R400, and L400, respectively. The result $\tilde{\epsilon}_{\text{ODT}}^{\text{ring}} > \tilde{\epsilon}_{\text{ODT}}^{\text{linear}}$ indicates that a stronger enthalpic repulsion between A and B monomers is needed to induce the order–disorder transition in diblock ring polymers. The ratio $\gamma^{\text{sim}} = \tilde{\epsilon}_{\text{ODT}}^{\text{ring}}/\tilde{\epsilon}_{\text{ODT}}^{\text{linear}} = 2.3 \pm 0.6$ for N = 50, while it is 2.9 ± 0.8 for N = 400. Leibler's RPA theory predicts $(\chi N)_{\text{ODT}}^{\text{linear}} = 10.5$, and Marko's RPA theory predicts $(\chi N)_{\text{ODT}}^{\text{ring}} = 17.8$. As such, the RPA theory predicts the ratio $\gamma^{\text{RPA}} = (\chi N)_{\text{ODT}}^{\text{ring}}/(\chi N)_{\text{ODT}}^{\text{linear}} = 17.8/10.5 = 1.7$. The simulation results deviate from the RPA theory prediction. Origins of the deviation include the non-

mean-field fluctuations near the ODT and the nonconcatenation topological constraints, both absent in the RPA theory. $\gamma^{\rm sim}$ for N=400 is higher than that for N=50 because the more compact globular conformations of large rings $(R_{\rm g}\sim N^{1/3})$ with respect to the Gaussian random-walk rings $(R_{\rm g}\sim N^{1/2})$ lead to more translational entropy loss per chain during phase separation. As a result, a higher χN is required to compensate for the translational entropy loss. Note that the conformational entropy of a block does not affect the ODT, as the conformation of the block is not perturbed much at the transition point.

Systematic uncertainty is associated with the two methods of estimating $\tilde{\epsilon}$. However, the ODTs for the diblock ring and linear polymers are studied using the same two methods, allowing a consistent comparison of their ODTs. The precise location of ODT may be determined using methods with reduced systematic uncertainties, such as well-tempered metadynamics simulations. ⁶⁴

The results of $\gamma^{\rm sim}$ are limited to N=50 and N=400, preventing us from systematically studying the N-dependence. However, they represent the short rings in Gaussian random-walk conformations and the long rings in more compact globular conformations. A comparison of the two is sufficient to demonstrate the effects of nonconcatenation on the phase-separation behavior of high-molecular-weight ring polymers. Simulations with more values of N are needed to clarify the N-dependence of $\gamma^{\rm sim}$ and stimulate the development of new theories as well.

3.3. Structure of Strongly Segregated Diblock Polymers. 3.3.1. Lamellar Spacing. As $\tilde{\epsilon}$ further increases above $\tilde{\epsilon}_{ODT}$, there is a strong segregation of the two blocks into their respective lamellar domains. The order parameter $\psi(\tilde{z})$ in the strong segregation regime reaches +1 or -1, indicating regions with pure A or B monomers. Strong segregation results in the extension of a polymer chain with respect to the unperturbed conformation at $\tilde{\epsilon}=0$. As a result, there is an increase of the lamellar spacing d with increasing $\tilde{\epsilon}$, as visualized in Figure 6a for R50 and Figure 7a for R400.

The lamellar spacing d in the strong segregation regime increases with $\tilde{\epsilon}$ for both the diblock ring and linear polymers, as shown in Figure 8. The values of d for each point in Figure 8 are listed in Tables S1–S6, Supporting Information. The increase with $\tilde{\epsilon}$ follows a power law $d \sim \tilde{\epsilon}^{\alpha}$ with the exponent $\alpha = 0.16 \pm 0.01$, 0.17 ± 0.01 , and 0.16 ± 0.01 for L400, R800, and R400, respectively. Theoretically, d is determined by

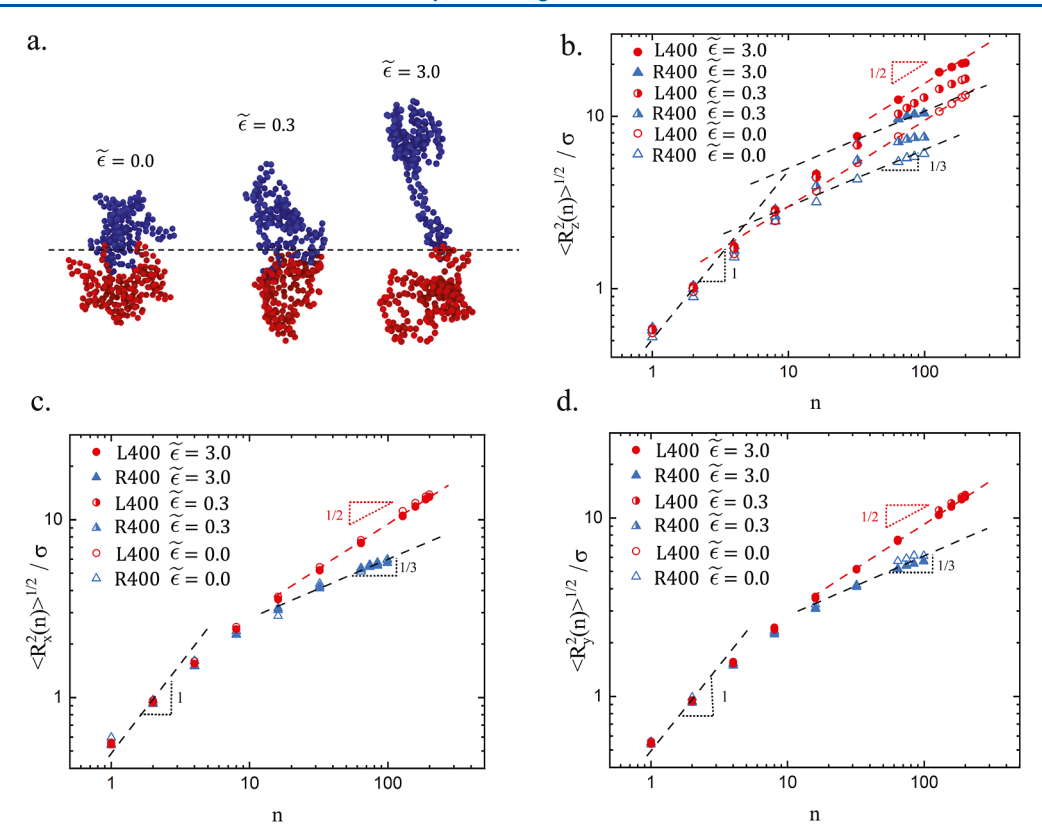


Figure 9. (a) Snapshots illustrating the conformational changes of a diblock ring polymer with increasing $\tilde{\epsilon}$ in the simulation sample R400. The dashed line indicates the plane of the diblock junction points. (b) Average z-component of the distance of a monomer from the junction of a diblock polymer $\langle R_z^2(n) \rangle^{1/2}$ as a function of the number of bonds n from the junction for N=400 at indicated $\tilde{\epsilon}$. (c) Average x-component $\langle R_z^2(n) \rangle^{1/2}$ and (d) y-component $\langle R_z^2(n) \rangle^{1/2}$ of the distance of a monomer from the junction.

balancing the enthalpic repulsion at the lamellar interface $F_{\rm enthalpic}$ and the entropic deformation energy of an extended diblock polymer $F_{\rm entropic}$. The interfacial tension is $\Gamma \approx \chi^{1/2} k_{\rm B} T/\sigma^2$, and the surface area per chain at the interface is A $\approx N\sigma^3/d$. As a result, the enthalpic repulsion is $F_{\rm enthalpic} \approx \Gamma A \approx$ $\chi^{1/2}k_{\rm B}TN\sigma/d$. The extension of a polymer from the unperturbed average size $\langle R_0 \rangle$ to a larger average size $\langle R \rangle$ results in $F_{
m entropic} pprox k_{
m B} T [\langle R \rangle / \langle R_0 \rangle]^2$. From $F_{
m enthalpic} pprox F_{
m entropic}$ one obtains $\langle R \rangle \sim \chi^{1/6}$. Since $\chi \sim \tilde{\epsilon}$ and $d \sim \langle R \rangle$, $d \sim \tilde{\epsilon}^{1/6}$. This scaling relation is indicated by the dashed line in Figure 8a. For L400, R800, and R400 in the simulations, the values of α all agree well with the theoretical prediction of $1/6 \approx 0.17$. The scaling argument originally developed for diblock linear polymers is applicable to diblock ring polymers because the entropic deformation energy of a diblock ring is also of the quadratic form $k_{\rm B}T[\langle R \rangle/\langle R_0 \rangle]^2$, as the ring polymer size distribution is Gaussian despite the fact that the average size $\langle R_0 \rangle$ depends on N differently from the linear polymer counterpart. 46 The theoretical value of α is not affected by the change in chain conformations from Gaussian random-walk coils to more compact globules. Numerically, one may use the component of the radius of gyration in the z-direction $R_{g,z}$ to quantify $\langle R \rangle$. As shown in Tables S1–S6, $d \approx 3R_{g,z}$ in all cases, agreeing with the scaling argument $d \sim \langle R \rangle$.

At the same \tilde{e} , d for R400 is smaller than d for L400, consistent with the ring polymers being more compact than the linear polymers, 28,33,35 i.e., $\langle R_0 \rangle^{\rm ring} < \langle R_0 \rangle^{\rm linear}$. Furthermore, d for R800 is also smaller than d for L400. The average size of diblock rings of N=800 is reduced compared with the

average size of diblock linear chains of N=400, indicating that R800 is not simply a ring that is double-folded around L400. The additional reduction with respect to the double-folded conformation is due to the topological constraints of nonconcatenation. Figure 8c visualizes R400, R800, and L400 with strong segregation at $\tilde{\epsilon}=3.0$, where the relative sizes of the diblock polymers are explicitly shown. For R100, where the effects of nonconcatenation have not emerged much, d is only slightly smaller than that for L50 at the same $\tilde{\epsilon}$ (see Figure 8a). For these shorter polymers, the increase in d with $\tilde{\epsilon}$ follows a weaker power law. $\alpha=0.11\pm0.01,\ 0.12\pm0.01,\$ and 0.14 ± 0.01 for L50, R100, and R200, respectively. The values of α are smaller than the theoretical value of $1/6\approx0.17$, reflecting the effects of finite chain size.

The N-dependence of d for the diblock ring polymers in the strong segregation regime is shown in Figure 8b. The increase follows another power law $d \sim N^{\nu}$ with the exponent $\nu = 0.63 \pm 0.01$, 0.61 ± 0.01 , 0.60 ± 0.01 , 0.61 ± 0.01 , and 0.60 ± 0.01 for $\tilde{e}=1.0$, 1.5, 2.0, 2.5, and 3.0, respectively. The theory based on the balance of the enthalpic repulsion $F_{\rm enthalpic}$ at the lamellar interface and the entropic deformation energy $F_{\rm entropic}$ can also predict the N-dependence of d for diblock rings. The scaling argument originally developed for diblock linear polymers is modified to account for the more compact globular conformations of diblock ring polymers. According to the fractal loopy globule model, the unperturbed average size of a diblock ring is $\langle R_0 \rangle \approx a(N/N_{\rm a})^{1/3}$, where $a \approx \sigma N_{\rm a}^{-1/2}$ is the average spacing between the topological constraints imposing on the diblock rings and equals the average size of a Gaussian

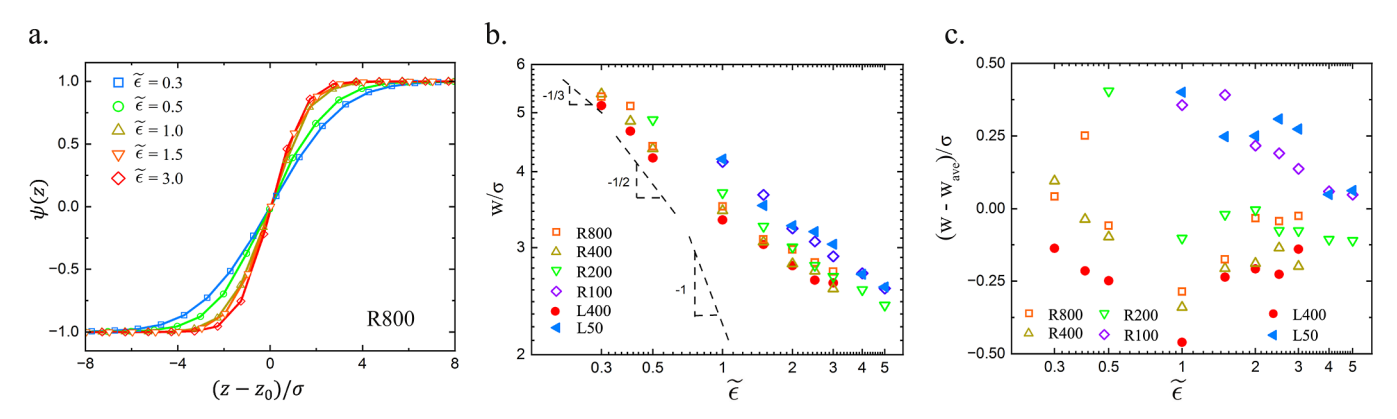


Figure 10. (a) Evolution of $\psi(z)$ with increasing interaction strength $\tilde{\epsilon}$ for R800 (symbols) and the best fit to the hyperbolic tangent function (lines). The best-fit value of z_0 is used to shift the profiles horizontally. (b) Interfacial width w as a function of $\tilde{\epsilon}$ for the indicated diblock copolymers. The dashed lines indicate the theoretical power-law dependence of the intrinsic interfacial width on the interaction strength in different scaling regimes. (c) $w - w_{ave}$ for the systems in (b). w_{ave} for each $\tilde{\epsilon}$ is the average of all w at the same $\tilde{\epsilon}$.

linear chain consisting of $N_{\rm a}$ beads of size σ . From $F_{\rm enthalpic} \approx F_{\rm entropic} \langle R \rangle \approx [\langle R_0 \rangle^2 \sigma N]^{1/3} \sim N^{5/9}$. The values of ν in Figure 8b are close to the theoretically predicted value of $5/9 \approx 0.56$, which is indicated by the dashed line.

3.3.2. Chain Conformations. Molecular simulations provide microscopic information that enables a detailed analysis of the diblock copolymer conformations. The evolution of the diblock ring conformation with increasing $ilde{arepsilon}$ is visualized in Figure 9a. The conformations of chain segments with one end at the junction point of a diblock polymer are characterized by their average end-to-end sizes in the x-, y-, and z-directions. Figure 9b shows the increase of the average end-to-end size in the z-direction $\langle R_z^2(n) \rangle^{1/2}$ as a function of the number of bonds n in the segment. For diblock linear polymers at $\tilde{\epsilon} = 0$, there is a crossover from $\langle R_z^2(n) \rangle^{1/2} \sim n$ to $\langle R_z^2(n) \rangle^{1/2} \sim n^{1/2}$ as the random-walk conformation develops with increasing n. By contrast, for diblock ring polymers at $\tilde{\epsilon}=0$, $\langle R_z^2(n)\rangle^{1/2} \sim n^{1/3}$ is developed at large n, indicating a more compact globular conformation. For both linear and ring polymers, as $\tilde{\epsilon}$ increases, the initial regime $\langle R_{\epsilon}^{2}(n) \rangle^{1/2} \sim n$, which corresponds to monomers in a rod-like conformation, extends to larger n. This change indicates the stretching of longer chain segments at the lamellar interface with an increasing enthalpic repulsion. The scaling $\langle R_*^2(n) \rangle^{1/2} \sim n^{1/2}$ and $\langle R_z^2(n) \rangle^{1/2} \sim n^{1/3}$ are eventually recovered for the stretched diblock linear and ring polymers, respectively. Figure 9b shows that the stretching accompanying the strong segregation of diblock polymers is not uniform along the polymer contour but instead located nearby the interface (small *n*) where A and B monomers can mix and interact. The values of block size normal to the interface R_z , which is defined as $\langle R_z^2(n=N/2)\rangle^{1/2}$ and $\langle R_z^2(n=N/4)\rangle^{1/2}$ for the diblock linear and ring polymers, respectively, are shown in Tables S1-S6. In all cases, the lamellar spacing d is comparable with $2R_z$ corresponding to the stacking of two neighboring layers of diblock copolymers in the lamellar domain.

The sizes of the segments in the x- and y-directions $\langle R_x^2(n) \rangle^{1/2}$ and $\langle R_y^2(n) \rangle^{1/2}$, respectively, are almost the same. Furthermore, Figure 9c,d shows there are almost no variations of $\langle R_x^2(n) \rangle^{1/2}$ and $\langle R_y^2(n) \rangle^{1/2}$ with increasing $\tilde{\epsilon}$. The crossover

from $\langle R_x^2(n) \rangle^{1/2} \sim n$ to $\langle R_x^2(n) \rangle^{1/2} \sim n^{1/2}$ for diblock linear chains and to $\langle R_x^2(n) \rangle^{1/2} \sim n^{1/3}$ for diblock rings are preserved, as are the counterparts for $\langle R_y^2(n) \rangle^{1/2}$. The independence of the in-plain polymer size on $\tilde{\epsilon}$ indicates that the strong segregation does not affect the chain conformations parallel to the lamellar interface. See Tables S1–S6 for the in-plane components of the radius of gyration $R_{g,x(y)}$ as well as the in-plane block sizes $R_{x(y)}$, which are defined as $\langle R_{x(y)}^2(n=N/2) \rangle^{1/2}$ and $\langle R_{x(y)}^2(n=N/4) \rangle^{1/2}$ for the diblock linear and ring polymers, respectively. Neither $R_{g,x(y)}$ nor $R_{x(y)}$ varies much with increasing $\tilde{\epsilon}$ in all systems.

3.3.3. Interfacial Width. As diblock polymers are stretched away from the interface with increasing \tilde{e} , the interfacial region where A and B monomers mix becomes narrower. This is seen in the change in the interfacial region that corresponds to the crossover from -1 to +1 in the order parameter profile. The narrowing of the interface with increasing enthalpic repulsion for R800 is shown in Figure 10a. The width of the interfacial region w is extracted from the order parameter profile by fitting it to $\psi(z) = \tanh[2(z-z_0)/w]$, where z_0 is the middle plane with $\phi_A = \phi_B = 0.5$. Best-fitting results are used for plotting the solid lines in Figure 10a. The best-fit values of w for different samples are plotted against \tilde{e} in Figure 10b.

Theoretically, it has been shown that $w \sim \chi^{-1/2}.^{16}$ The derivation was based on equating the enthalpic penalty $g\chi k_{\rm B}T$ of a g-monomer segment that enters the opposite side of the interface and the thermal energy $k_{\rm B}T$, which results in $g \sim \chi^{-1}$. The g-monomer segment was described as a Gaussian randomwalk coil with an average size of $r \sim g^{1/2}$. The argument $w \approx r$ then gave $w \sim \chi^{-1/2}$. A deviation of the g-monomer segment conformation from the Gaussian random-walk coil results in a breakdown of the scaling argument. If the segments are sufficiently short, they are in rod-like conformations. The average size of the g-monomer segment is $r_g \sim g \sim \chi^{-1}$, and $w \approx r_g \sim \chi^{-1}$. For diblock ring polymers, if the segments are sufficiently long, they are in fractal globular conformations. The average size is $r_g \sim g^{1/3} \sim \chi^{-1/3}$, and $w \approx r_g \sim \chi^{-1/3}$. Based on the two new scaling regimes, a modified theoretical prediction is as follows:

(1) For diblock linear chains, there is a crossover from $w \sim \chi^{-1/2}$ to $w \sim \chi^{-1}$ as χ is large enough to make w smaller than the persistence length $l_{\rm p}$ of the polymer.

(2) For diblock rings, there is a second crossover from $w \sim \chi^{-1/3}$ to $w \sim \chi^{-1/2}$ as w drops below the average spacing a between the topological constraints, in addition to the crossover from $w \sim \chi^{-1/2}$ to $w \sim \chi^{-1}$ as w drops below l_p .

The new theoretical predictions are indicated by the dashed lines in Figure 10b and compared to the simulation data. All simulation values of w in Figure 10b are comparable to or smaller than $a \approx 5\sigma$. Therefore, regime $w \sim \chi^{-1/3}$ and its crossover to regime $w \sim \chi^{-1/2}$ are irrelevant to the interpretation of the simulation data. The range $w < l_p \approx 3\sigma$ is covered by the simulations. As a result, regime $w \sim \chi^{-1}$ and the crossover to it from regime $w \sim \chi^{-1/2}$ are relevant. Figure 10b shows a significantly less rapid decrease of w with increasing χ when compared with the predicted regimes $w \sim \chi^{-1/2}$ and $w \sim \chi^{-1}$. Such a deviation from the theory is attributed to the capillary-wave-induced broadening of the interface.

One example of the broadening of a lamellar interface due to the capillary wave is given in Figure S1, Supporting Information. The example is for the sample R400 at $\tilde{e}=0.5$. The simulation box is divided into 10 columnar subregions, each corresponding to $(L_x/10) \times L_y$ in the xy-plane. Each of the 10 order parameter profiles $\psi(\tilde{z})$ for the 10 subregions is well fitted to the hyperbolic tangent function. However, the middle-plane position z_0 varies from one subregion to another, indicating the existence of a capillary wave. The average of the individual w in each subregion is 3.9σ . It is smaller than $w=4.9\sigma$ of the average order-parameter profile for all subregions by 1σ .

The example above is for one particular $\tilde{\epsilon}$ at one particular resolution of length scale along one particular direction. Completing a similar analysis for all values of $\tilde{\epsilon}$ and all wavelengths along all directions would require much more work. Note that the wavelength is cut at the finite simulation box size, and examining longer capillary wavelengths would require a sample with a larger interfacial area.

As a characterization of the local interfacial structure, the interfacial width is expected to be independent of the chain length or topology. This independence is indeed the prediction in theory for the intrinsic interfacial width. However, the values of w for different samples in the simulations are not identical at the same $\tilde{\epsilon}$, as shown in Figure 10b. This is attributed to the effects of the capillary wave. The molecular weight dependence of the capillary wave effects has been theoretically and computationally studied, ^{66,68} but the role of nonconcatenation ring topology in a capillary wave needs future work to clarify. Despite the variation of w with chain length and topology, the magnitude of the variation is small. Figure 10c shows the variation of w with respect to w_{ave} , which is the average for different samples at the same $\tilde{\epsilon}$, is smaller than the coarse-grained bead size σ .

4. CONCLUDING REMARKS

Large-scale molecular simulations of diblock copolymers with $N/N_{\rm e}$ up to O(10) have been performed to examine the effects of nonconcatenated ring topology on the phase behavior of high-molecular-weight diblock copolymers. The nonconcatenated ring topology affects both the order—disorder transition and the structure of the ordered lamellar phase of symmetric diblock copolymers. The key findings of the simulations are listed below with some remarks.

- (1) The relatively faster dynamics of nonconcatenated ring polymers, which is due to the lack of a long-lived entanglement network, facilitates the kinetics of phase separation in the simulations. While a bond-swap MC algorithm may be used to bypass the entanglement network and accelerate the kinetics of phase separation of diblock linear polymers in molecular simulations, no such artificial moves may be achieved in real experiments. As such, the faster phase separation in diblock rings provides a topology-based pathway to facilitate the processing of diblock polymers.
- (2) The nonconcatenation topology forces the diblock ring polymers to be in globular conformations that are more compact than Gaussian random-walk coils. As a result, the translational entropy lost in the transition from the disorder phase to the lamellar phase is more than that for Gaussian diblock ring polymers, shifting the transition to a higher strength of enthalpic repulsion. The simulations s h o w $\gamma^{\rm sim} = \tilde{\epsilon}_{\rm ODT}^{\rm ring}/\tilde{\epsilon}_{\rm ODT}^{\rm linear} = 2.9 \pm 0.8$ for $N = 400(14N_{\rm e})$ is higher than $\gamma^{\rm sim} = 2.3 \pm 0.6$ for $N = 50(1.8N_{\rm e})$. However, both γ^{sim} are larger than the predicted $\gamma^{\text{RPA}} =$ 1.7 of the mean-field RPA theory. Future development of a phase-separation theory for diblock ring polymers needs to incorporate the topological invariants of nonconcatenation as well as the effects of fluctuations in order to match the sophistication of the field theories for linear 16,22 and Gaussian ring polymers. 69,70 The more significant deviation of the structure factor $S_0(q)$ in the disorder phase from the predictions of Marko's RPA theory (Figure 4b), when compared with the counterpart for diblock linear polymers (Figure 4a), also call for a new theory for diblock rings.
- (3) In the strong segregation regime, the increases of the lamellar spacing d with the strength of enthalpic repulsion and the molecular weight of polymer follow the respective power laws $d \sim \tilde{e}^{\alpha}$ and $d \sim N^{\nu}$. The theoretical argument $F_{\text{enthalpic}} \approx F_{\text{entropic}}$ predicts $\alpha = 1/6$, regardless of the copolymer topology. α in the simulations of L400, R800, and R400 agree well with the theoretical prediction, while α for L50, R100, and R200 are noticeably smaller. Incorporating the scaling relation for the fractal globular conformation of ring polymers into the theoretical argument further predicts ν = 5/9, which describes the simulation data. At the same $ilde{\epsilon}$, $d_{
 m R800}$ < $d_{
 m L400}$, reflecting the more compact conformation of nonconcatenated diblock rings with respect to the conformation double folded around a Gaussian linear chain. The reduced lamellar spacing in the lamellar phase of diblock ring polymers has been observed experimentally.²⁶ Future experiments may aim for a more quantitative examination of how lamellar spacing depends on control parameters.
- (4) Strongly segregated diblock copolymers are not uniformly stretched but localized near the interface, as revealed by the plot of $\langle R_z^2(n) \rangle^{1/2}$. The extension normal to the interface has no effects on the polymer conformations within the interface plane, as quantified by $\langle R_x^2(n) \rangle^{1/2}$ and $\langle R_y^2(n) \rangle^{1/2}$. This microscopic detail could help to develop a theory beyond the scaling argument to model the structure of the lamellar interface.

(5) For strong segregation, the order parameter profile across the lamellar interface is fitted well by the hyperbolic tangent function. The width of the lamellar interface w is reduced with increasing \tilde{e} as the enthalpic repulsion penalizes the mixing of two blocks. The reduction in w is less rapid than predicted by the theory because the capillary wave broadens w with respect to the intrinsic interfacial width. At the same \tilde{e} , w exhibits slight variation with chain length and topology (smaller than 1σ in the simulations). The subtle effects of the capillary wave on w is a good topic for future research.

It is anticipated that the ingenious synthesis and precise characterization of high-molecular-weight homopolymer rings 48,49 may be extended to create diblock ring polymers and thus propel experimental research on the phase behavior of diblock rings. The study of diblock ring polymer phase behavior could be also stretched to help reflect on the rich features of chromatin organization in the cell nucleus, where abundant loops are present.⁷¹

ASSOCIATED CONTENT

Supporting Information

The Supporting Information is available free of charge at https://pubs.acs.org/doi/10.1021/acs.macromol.3c02473.

Components of the radius of gyration and block sizes in the x-, y-, and z-directions for L50, R100, R200, R400, R800, and L400 and order parameter profiles demonstrating the capillary wave for R400 (PDF)

AUTHOR INFORMATION

Corresponding Author

Ting Ge — Department of Chemistry and Biochemistry, University of South Carolina, Columbia, South Carolina 29208, United States; ⊚ orcid.org/0000-0003-2456-732X; Email: tingg@mailbox.sc.edu

Authors

Andrew Wijesekera – Department of Chemistry and Biochemistry, University of South Carolina, Columbia, South Carolina 29208, United States; orcid.org/0009-0006-1591-9046

Daniel L. Vigil — Sandia National Laboratories, Albuquerque, New Mexico 87185, United States; orcid.org/0000-0001-9860-0888

Complete contact information is available at: https://pubs.acs.org/10.1021/acs.macromol.3c02473

Notes

The authors declare no competing financial interest.

ACKNOWLEDGMENTS

We thank G. S. Grest, T. C. O'Connor, and M. Stefik for helpful discussions. T.G. acknowledges start-up funds from the University of South Carolina and the National Science Foundation CAREER award DMR-2236693. Computational resources were provided by University of South Carolina flagship computing cluster Hyperion. This work was performed, in part, at the Center for Integrated Nanotechnologies, an Office of Science User Facility operated for the U.S. Department of Energy (DOE) Office of Science. Sandia National Laboratories is a multimission laboratory managed and operated by National Technology and Engineer-

ing Solutions of Sandia, LLC, a wholly owned subsidiary of Honeywell International, Inc., for the U.S. DOE's National Nuclear Security Administration under Contract No.DE-NA-0003525. The views expressed in the paper do not necessarily represent the views of the U.S. DOE or the U.S. Government.

REFERENCES

- (1) Lodge, T. P. Block copolymers: Past successes and future challenges. *Macromol. Chem. Phys.* **2003**, 204, 265–273.
- (2) Segalman, R. A. Patterning with block copolymer thin films. *Mater. Sci. Eng., R* **2005**, *48*, 191–226.
- (3) Hillmyer, M. A. Nanoporous materials from block copolymer precursors. *Adv. Polym. Sci.* **2005**, *190*, 137–181.
- (4) Bates, C. M.; Bates, F. S. 50th anniversary perspective: Block polymers pure potential. *Macromolecules* **2017**, *50*, 3–22.
- (Ś) Weller, D. W.; Ma, G.; Galuska, L. A.; Zhang, S.; Stringer, M.; Aracri, S.; Wang, W.; Hong, K.; Gu, X. Strain-Induced Nanocavitation in Block Copolymer Thin Films for High Performance Filtration Membranes. ACS Appl. Polym. Mater. 2021, 3, 5666–5673.
- (6) Nian, S.; Fan, Z.; Freychet, G.; Zhernenkov, M.; Redemann, S.; Cai, L. H. Self-Assembly of Flexible Linear-Semiflexible Bottlebrush-Flexible Linear Triblock Copolymers. *Macromolecules* **2021**, *54*, 9361–9371.
- (7) Helfand, E. Theory of inhomogeneous polymers: Fundamentals of the Gaussian random-walk model. *J. Chem. Phys.* **1975**, *62*, 999–1005
- (8) Leibler, L. Theory of Microphase Separation in Block Copolymers. *Macromolecules* **1980**, *13*, 1602–1617.
- (9) Semenov, A. N. Contribution to the theory of microphase layering in block-copolymer melts. Sov. Phys. JETP 1985, 61, 733.
- (10) Fredrickson, G. H.; Helfand, E. Fluctuation effects in the theory of microphase separation in block copolymers. *J. Chem. Phys.* **1987**, 87, 697–705.
- (11) Olvera de la Cruz, M. Theory of microphase separation in block copolymer solutions. *J. Chem. Phys.* **1989**, *90*, 1995–2002.
- (12) Mayes, A. M.; de la Cruz, M. O. Concentration fluctuation effects on disorder-order transitions in block copolymer melts. *J. Chem. Phys.* **1991**, 95, 4670–4677.
- (13) Marko, J. F. Microphase Separation of Block Copolymer Rings. *Macromolecules* **1993**, 26, 1442–1444.
- (14) Matsen, M. W.; Bates, F. S. Unifying weak- and strong-segregation block copolymer theories. *Macromolecules* **1996**, *29*, 1091–1098.
- (15) Ganesan, V.; Fredrickson, G. H. Field-theoretic polymer simulations. *Europhys. Lett.* **2001**, *55*, 814–820.
- (16) Fredrickson, G. The Equilibrium Theory of Inhomogeneous Polymers. Oxford University Press, 2006.
- (17) Yu, B.; Sun, P.; Chen, T.; Jin, Q.; Ding, D.; Li, B.; Shi, A. C. Confinement-Induced Novel Morphologies of Block Copolymers. *Phys. Rev. Lett.* **2006**, *96*, 138306.
- (18) Qin, J.; Morse, D. C. Fluctuations in symmetric diblock copolymers: Testing theories old and new. *Phys. Rev. Lett.* **2012**, *108*, 238301.
- (19) Shi, A.-C. Self-Consistent Field Theory of Inhomogeneous Polymeric Systems: A Variational Derivation. *Adv. Theory Simul.* **2019**, *2*, 1800188.
- (20) Zhulina, E. B.; Sheiko, S. S.; Borisov, O. V. Theory of Microphase Segregation in the Melts of Copolymers with Dendritically Branched, Bottlebrush, or Cycled Blocks. *ACS Macro Lett.* **2019**, *8*, 1075–1079.
- (21) Zhulina, E. B.; Sheiko, S. S.; Dobrynin, A. V.; Borisov, O. V. Microphase Segregation in the Melts of Bottlebrush Block Copolymers. *Macromolecules* **2020**, *53*, 2582–2593.
- (22) Matsen, M. W. Field theoretic approach for block polymer melts: SCFT and FTS. J. Chem. Phys. 2020, 152, 152.
- (23) Iatrou, H.; Hadjichristidis, N.; Meier, G.; Frielinghaus, H.; Monkenbusch, M. Synthesis and characterization of model cyclic block copolymers of styrene and butadiene. Comparison of the

- aggregation phenomena in selective solvents with linear diblock and triblock analogues. *Macromolecules* **2002**, *35*, 5426–5437.
- (24) Zhu, Y.; Gido, S. P.; Iatrou, H.; Hadjichristidis, N.; Mays, J. W. Microphase separation of cyclic block copolymers of styrene and butadiene and of their corresponding linear triblock copolymers. *Macromolecules* **2003**, *36*, 148–152.
- (25) Matsushita, Y.; Iwata, H.; Asari, T.; Uchida, T.; ten Brinke, G.; Takano, A. Chain elongation suppression of cyclic block copolymers in lamellar microphase-separated bulk. *J. Chem. Phys.* **2004**, *121*, 1129–1132.
- (26) Poelma, J. E.; Ono, K.; Miyajima, D.; Aida, T.; Satoh, K.; Hawker, C. J. Cyclic block copolymers for controlling feature sizes in block copolymer lithography. *ACS Nano* **2012**, *6*, 10845–10854.
- (27) Gartner, T. E.; Kubo, T.; Seo, Y.; Tansky, M.; Hall, L. M.; Sumerlin, B. S.; Epps, T. H. Domain Spacing and Composition Profile Behavior in Salt-Doped Cyclic vs Linear Block Polymer Thin Films: A Joint Experimental and Simulation Study. *Macromolecules* **2017**, *50*, 7169–7176.
- (28) Halverson, J. D.; Lee, W. B.; Grest, G. S.; Grosberg, A. Y.; Kremer, K. Molecular dynamics simulation study of nonconcatenated ring polymers in a melt. I. Statics. *J. Chem. Phys.* **2011**, *134*, 204904.
- (29) Sakaue, T. Ring polymers in melts and solutions: Scaling and crossover. *Phys. Rev. Lett.* **2011**, *106*, 167802.
- (30) Rosa, A.; Everaers, R. Ring Polymers in the Melt State: The Physics of Crumpling. *Phys. Rev. Lett.* **2014**, *112*, 118302.
- (31) Obukhov, S.; Johner, A.; Baschnagel, J.; Meyer, H.; Wittmer, J. P. Melt of polymer rings: The decorated loop model. *Europhys. Lett.* **2014**, *105*, 48005.
- (32) Smrek, J.; Grosberg, A. Y. Minimal Surfaces on Unconcatenated Polymer Rings in Melt. ACS Macro Lett. **2016**, *5*, 750–754.
- (33) Ge, T.; Panyukov, S.; Rubinstein, M. Self-Similar Conformations and Dynamics in Entangled Melts and Solutions of Nonconcatenated Ring Polymers. *Macromolecules* **2016**, 49, 708–722.
- (34) Smrek, J.; Kremer, K.; Rosa, A. Threading of Unconcatenated Ring Polymers at High Concentrations: Double-Folded vs Time-Equilibrated Structures. ACS Macro Lett. **2019**, 8, 155–160.
- (35) Kruteva, M.; Allgaier, J.; Monkenbusch, M.; Porcar, L.; Richter, D. Self-Similar Polymer Ring Conformations Based on Elementary Loops: A Direct Observation by SANS. *ACS Macro Lett.* **2020**, *9*, 507–511.
- (36) Kapnistos, M.; Lang, M.; Vlassopoulos, D.; Pyckhout-Hintzen, W.; Richter, D.; Cho, D.; Chang, T.; Rubinstein, M. Unexpected power-law stress relaxation of entangled ring polymers. *Nat. Mater.* **2008**, *7*, 997–1002.
- (37) Halverson, J. D.; Lee, W. B.; Grest, G. S.; Grosberg, A. Y.; Kremer, K. Molecular dynamics simulation study of nonconcatenated ring polymers in a melt. II. Dynamics. *J. Chem. Phys.* **2011**, *134*, 204905.
- (38) Michieletto, D.; Marenduzzo, D.; Orlandini, E.; Alexander, G. P.; Turner, M. S. Dynamics of self-threading ring polymers in a gel. *Soft Matter* **2014**, *10*, 5936–5944.
- (39) Tsalikis, D. G.; Mavrantzas, V. G.; Vlassopoulos, D. Analysis of Slow Modes in Ring Polymers: Threading of Rings Controls Long-Time Relaxation. *ACS Macro Lett.* **2016**, *5*, 755–760.
- (40) Ge, T.; Grest, G. S.; Rubinstein, M. Nanorheology of Entangled Polymer Melts. *Phys. Rev. Lett.* **2018**, *120*, 057801.
- (41) Huang, Q.; Ahn, J.; Parisi, D.; Chang, T.; Hassager, O.; Panyukov, S.; Rubinstein, M.; Vlassopoulos, D. Unexpected Stretching of Entangled Ring Macromolecules. *Phys. Rev. Lett.* **2019**, 122, 208001.
- (42) Kruteva, M.; Monkenbusch, M.; Allgaier, J.; Holderer, O.; Pasini, S.; Hoffmann, I.; Richter, D. Self-Similar Dynamics of Large Polymer Rings: A Neutron Spin Echo Study. *Phys. Rev. Lett.* **2020**, 125, 238004.
- (43) Zhang, K.; Lackey, M. A.; Cui, J.; Tew, G. N. Gels based on cyclic polymers. *J. Am. Chem. Soc.* **2011**, *133*, 4140–4148.
- (44) Romio, M.; Trachsel, L.; Morgese, G.; Ramakrishna, S. N.; Spencer, N. D.; Benetti, E. M. Topological Polymer Chemistry Enters

- Materials Science: Expanding the Applicability of Cyclic Polymers. ACS Macro Lett. 2020, 9, 1024–1033.
- (45) Parisi, D.; Costanzo, S.; Jeong, Y.; Ahn, J.; Chang, T.; Vlassopoulos, D.; Halverson, J. D.; Kremer, K.; Ge, T.; Rubinstein, M.; Grest, G. S.; Srinin, W.; Grosberg, A. Y. Nonlinear Shear Rheology of Entangled Polymer Rings. *Macromolecules* **2021**, *54*, 2811–2827.
- (46) Wang, J.; O'Connor, T. C.; Grest, G. S.; Ge, T. Superstretchable Elastomer from Cross-linked Ring Polymers. *Phys. Rev. Lett.* **2022**, *128*, 237801.
- (47) Singh, M.; Dong, M.; Wu, W.; Nejat, R.; Tran, D. K.; Pradhan, N.; Raghavan, D.; Douglas, J. F.; Wooley, K. L.; Karim, A. Enhanced Dielectric Strength and Capacitive Energy Density of Cyclic Polystyrene Films. *ACS Polym. Au* **2022**, *2*, 324–332.
- (48) Haque, F. M.; Grayson, S. M. The synthesis, properties and potential applications of cyclic polymers. *Nat. Chem.* **2020**, *12*, 433–444.
- (49) Yoon, K. Y.; Noh, J.; Gan, Q.; Edwards, J. P.; Tuba, R.; Choi, T. L.; Grubbs, R. H. Scalable and continuous access to pure cyclic polymers enabled by 'quarantined' heterogeneous catalysts. *Nat. Chem.* **2022**, *14*, 1242–1248.
- (50) Goodson, A. D.; Troxler, J. E.; Rick, M. S.; Ashbaugh, H. S.; Albert, J. N. Impact of Cyclic Block Copolymer Chain Architecture and Degree of Polymerization on Nanoscale Domain Spacing: A Simulation and Scaling Theory Analysis. *Macromolecules* **2019**, *52*, 9389–9397.
- (51) Herschberg, T.; Carrillo, J. M. Y.; Sumpter, B. G.; Panagiotou, E.; Kumar, R. Topological Effects near Order-Disorder Transitions in Symmetric Diblock Copolymer Melts. *Macromolecules* **2021**, *54*, 7492–7499.
- (52) Kremer, K.; Grest, G. S. Dynamics of entangled linear polymer melts: A molecular-dynamics simulation. *J. Chem. Phys.* **1990**, *92*, 5057–5086.
- (53) Everaers, R.; Sukumaran, S. K.; Grest, G. S.; Svaneborg, C.; Sivasubramanian, A.; Kremer, K. Rheology and Microscopic Topology of Entangled Polymeric Liquids. *Science* **2004**, *303*, 823–826.
- (54) Grest, G. S. Communication: Polymer entanglement dynamics: Role of attractive interactions. *J. Chem. Phys.* **2016**, *145*, 141101.
- (55) Grest, G. S.; Lacasse, M. D.; Kremer, K.; Gupta, A. M. Efficient continuum model for simulating polymer blends and copolymers. *J. Chem. Phys.* **1996**, *105*, 10583–10594.
- (56) Murat, M.; Grest, G. S.; Kremer, K. Lamellar block copolymers: Diffusion and reduction of entanglement effects. *Europhys. Lett.* **1998**, 42, 401–406.
- (57) Murat, M.; Grest, G. S.; Kremer, K. Statics and Dynamics of Symmetric Diblock Copolymers: A Molecular Dynamics Study. *Macromolecules* **1999**, *32*, 595–609.
- (58) Grest, G. S.; Ge, T.; Plimpton, S. J.; Rubinstein, M.; O'Connor, T. C. Entropic Mixing of Ring/Linear Polymer Blends. *ACS Polym. Au* **2023**, *3*, 209–216.
- (59) Zhang, W.; Gomez, E. D.; Milner, S. T. Predicting Flory-Huggins χ from Simulations. *Phys. Rev. Lett.* **2017**, *119*, 017801.
- (60) Glaser, J.; Medapuram, P.; Beardsley, T. M.; Matsen, M. W.; Morse, D. C. Universality of block copolymer melts. *Phys. Rev. Lett.* **2014**, *113*, 068302.
- (61) Sides, S. W.; Grest, G. S.; Stevens, M. J.; Plimpton, S. J. Effect of End-Tethered Polymers on Surface Adhesion of Glassy Polymers. *J. Polym. Sci., Part B: Polym. Phys.* **2004**, 42, 199–208.
- (62) Thompson, A. P.; Aktulga, H. M.; Berger, R.; Bolintineanu, D. S.; Brown, W. M.; Crozier, P. S.; in 't Veld, P. J.; Kohlmeyer, A.; Moore, S. G.; Nguyen, T. D.; Shan, R.; Stevens, M. J.; Tranchida, J.; Trott, C.; Plimpton, S. J. LAMMPS-a flexible simulation tool for particle-based materials modeling at the atomic, meso, and continuum scales. *Comput. Phys. Commun.* **2022**, 271, 108171.
- (63) Rottler, J.; Müller, M. Kinetic Pathways of Block Copolymer Directed Self-Assembly: Insights from Efficient Continuum Modeling. *ACS Nano* **2020**, *14*, 13986–13994.

- (64) Ghasimakbari, T.; Morse, D. C. Order-Disorder Transitions and Free Energies in Asymmetric Diblock Copolymers. *Macromolecules* **2020**, *53*, 7399–7409.
- (65) Werner, A.; Schmid, F.; Müller, M.; Binder, K. Anomalous size-dependence of interfacial profiles between coexisting phases of polymer mixtures in thin-film geometry: A Monte Carlo simulation. *J. Chem. Phys.* **1997**, *107*, 8175–8188.
- (66) Lacasse, M. D.; Grest, G. S.; Levine, A. J. Capillary-Wave and Chain-Length Effects at Polymer/Polymer Interfaces. *Phys. Rev. Lett.* **1998**, *80*, 309–312.
- (67) Vink, R. L. C.; Horbach, J.; Binder, K. Capillary waves in a colloid-polymer interface. *J. Chem. Phys.* **2005**, *122*, 134905.
- (68) Semenov, A. N. Scattering of Statistical Structure of Polymer/Polymer Interfaces. *Macromolecules* **1994**, 27, 2732–2735.
- (69) Kim, J. U.; Yang, Y. B.; Lee, W. B. Self-consistent field theory of gaussian ring polymers. *Macromolecules* **2012**, *45*, 3263–3269.
- (70) Qiang, Y.; Li, W. Accelerated Method of Self-Consistent Field Theory for the Study of Gaussian Ring-Type Block Copolymers. *Macromolecules* **2021**, *54*, 9071–9078.
- (71) Chan, B.; Rubinstein, M. Theory of chromatin organization maintained by active loop extrusion. *Proc. Natl. Acad. Sci. U.S.A.* **2023**, 120, No. e2222078120.